

Data space inversion for efficient uncertainty quantification using an integrated surface and subsurface hydrologic model

Hugo Delottier¹, John Doherty² and Philip Brunner¹

5 ¹ Centre for Hydrogeology and Geothermics (CHYN), University of Neuchâtel, Neuchâtel, Switzerland

² Watermark Numerical Computing, Corinda, QLD, Australia

Correspondence to: Hugo Delottier (hugo.delottier@unine.ch)

Abstract. It is incumbent on decision-support hydrological modelling to make predictions of uncertain quantities in a decision-support context. In implementing decision-support modelling, data assimilation and uncertainty quantification are often the most difficult and time-consuming tasks. This is because the imposition of history-matching constraints on model parameters usually requires a large number of model runs. Data Space Inversion (DSI) provides a highly model-run-efficient method for predictive uncertainty quantification. It does this by evaluating covariances between model outputs used for history matching (e.g. hydraulic heads) and model predictions based on model runs that sample the prior parameter probability distribution. By directly focusing on the relationship between model outputs under historical conditions and predictions of system behaviour under future conditions, DSI avoids the need to estimate or adjust model parameters. This is advantageous when using Integrated Surface and Subsurface Hydrologic Models (ISSHMs) because these models are associated with long run times and numerical instability, and/or complex parameterisation schemes that are designed to respect geological realism. This paper demonstrates that DSI provides a robust and efficient means of quantifying the uncertainties of complex model predictions. At the same time, DSI provides a basis for complementary linear analysis that allows to explore the worth of available observations, as well as of observations which are yet to be acquired. This allows for the design of highly efficient, future data acquisition campaigns. DSI is applied in conjunction with an ISSHM representing a synthetic but realistic river-aquifer system. Predictions of interest are fast travel times and surface water infiltration. Linear and nonlinear estimates of predictive uncertainty based on DSI are validated against a more traditional uncertainty quantification which requires adjustment of a large number of parameters. A DSI-generated surrogate model is then used to investigate the effectiveness and efficiency of existing and possible future monitoring networks. The example demonstrates the benefits of using DSI in conjunction with a complex numerical model to quantify predictive uncertainty and support data worth analysis in complex hydrogeological environments.

1. Introduction

35

Numerical hydrological models are often built to make predictions that support decision-making. In this paper we use the term “prediction” to refer to any quantity of management interest calculated by a numerical model, whether it is estimated in the future or is a by-product of data assimilation. Generally, Bayesian methods are applied to models so that the uncertainties associated with predictions of management interest can be quantified and reduced. Through this process, the prior uncertainties of these predictions are constrained by the assimilation of observations to provide estimates of posterior predictive uncertainties. A variety of Bayesian methods are available for this purpose. These include linear methods (James et al., 2009; Dausman et al., 2010), linear-assisted methods such as null-space Monte Carlo (Tonkin and Doherty 2009; Doherty 2015) and nonlinear methods such as Markov chain Monte Carlo (see, for example, Vrugt 2016). More recently, ensemble methods such as those described by Chen and Oliver (2013) and White (2018) have been used in this context. The attractiveness of ensemble methods lies in their ability to accommodate a large number of parameters with a high degree of model run efficiency.

40

45

50

In many hydrogeological settings, geological structures such as elongate structural or alluvial features that embody interconnected permeability are of high conceptual relevance as they can have a major impact on management-salient predictions. Representation of these features typically requires the use of categorical parameterisation schemes that maintain their relation and connectivity in space. Despite the efficiency of ensemble methods, it is difficult for them to adjust and maintain permeability connectedness as parameter fields are adjusted so that model outputs can respect field measurements (Lam et al., 2020; Juda et al., 2022). Additionally, theoretical problems arise from the multi-Gaussian assumption on which ensemble methods are based. Practical problems arise from the sometimes problematic behaviour of complex numerical models when endowed with stochastic parameter fields with high contrasts in hydraulic conductivity. These problems are generally exacerbated when solute transport is simulated in addition to flow. It follows that the use of model partner software such as PEST (Doherty 2022) and PESTPP-IES (White 2018) for parameter field conditioning and predictive uncertainty analysis and reduction is not always feasible. This makes it difficult to maintain the simulation integrity of physically based numerical models where potentially information-rich site data must be assimilated. Compromises in model structure, parameterisation or process complexity may therefore be required (see, for example, Delottier et al., 2022).

55

60

65

70

To overcome these problems, methods have been developed to generate posterior distributions of predictions without the need to adjust the complex parameter fields of large, physically based numerical models (for example Satija and Caers 2015; He et al., 2018; Hermans 2017; Sun and Durlafsky 2017). Computational advantages are gained by establishing a direct link between historical observations of system behaviour and predictions of interest. To establish this link, a numerical model of arbitrary process complexity is used. This model is equipped with parameter fields that can best express the hydrogeological characteristics of the simulated system. These may include complex structures that represent heterogeneous, three-dimensional configurations of hydraulic properties. Because no adjustment of the parameter fields is required, simulation integrity is maintained regardless of the complexity of hydrogeological site conceptualisation. Instead, the model is used to build a prior probability distribution of predictions of interest based on samples of realistic hydraulic

75 property fields. The same model runs that are used to explore prior predictive uncertainty are used to construct a joint probability distribution that links historical system behaviour with future system behaviour.

Some of the methods that adopt this approach to posterior predictive uncertainty analysis attempt to develop explicit relationships between historical observations of system behaviour on the one hand and predictions of
80 future system behaviour on the other hand (Satija and Caers 2015; Scheidt et al. 2015). In contrast, other methods develop a more implicit relationship between these two (Sun and Durlofsky 2017; Lima et al. 2020). Once these relationships have been established, predictions of interest can be directly conditioned by real-world measurements of historical system behaviour. The need for manipulation and estimation of parameters is thereby obviated. Consequently, the numerical burden of predictive uncertainty reduction and quantification is
85 significantly reduced, regardless of the complexity of the numerical model and regardless of the complexity of the prior parameter probability distribution.

In this paper, we employ a “data space inversion” (i.e. DSI) methodology that is similar to that described by Lima et al. (2020). At the same time, we extend the methodology to consider the worth of existing and future
90 data. Assessment of data worth is based on the premise that the value of data increases with its ability to reduce the uncertainties of predictions. Because it requires uncertainty quantification, assessing the worth of data using methods that rely on explicit or implicit (through linear analysis) parameter adjustment can be computationally expensive, especially when performed in numerical and parameterisation contexts that attempt to respect hydrogeological processes and hydraulic property integrity. The numerically inexpensive methodology for data
95 worth assessment that is presented herein can support these assessments in modelling contexts where it would otherwise be computationally intractable. The proposed approach is therefore especially attractive for Integrated Surface and Subsurface Hydrologic Models (ISSHMs). Thus it can support attempts to achieve the goals of decision-support utility and failure avoidance that are set out in articles such as Kikuchi 2017 and Doherty and Moore 2020.

100

All of the methods described here can be applied using PEST (Doherty, 2022) and/or PEST++ (PEST++ Development Team, 2022). They are therefore readily available to the wider modelling community.

The paper is organised as follows: Section 2 describes the theory behind DSI. In the ensuing section, a synthetic
105 alluvial river-aquifer system is introduced. This is then used to (i) validate DSI estimates of predictive uncertainty and (ii) demonstrate the use of DSI in quantifying the worth of existing and new data in reducing predictive uncertainty.

2. Theory

110

2.1 Statistical Linkage between the Past and the Future

Let the vector \mathbf{o} denote outputs of a model that correspond to field measurements of system behaviour (e.g. system states and fluxes). Meanwhile, we denote the actual field measurements of these quantities by the vector

115 \mathbf{h} . We use the symbol \mathbf{Z} to characterise the operator through which model outputs \mathbf{o} are calculated from model parameters; the latter are denoted by the vector \mathbf{k} . Therefore:

$$\mathbf{h} = \mathbf{o} + \boldsymbol{\varepsilon} = \mathbf{Z}(\mathbf{k}) + \boldsymbol{\varepsilon} \quad (1)$$

The vector $\boldsymbol{\varepsilon}$ denotes the noise associated with field measurements \mathbf{h} . It may also include the model-to-
120 measurement misfit which arises from the imperfect nature of numerical simulation. In the present case we combine both of these into a single “noise” term. It is generally assumed that $\boldsymbol{\varepsilon}$ has a mean of $\mathbf{0}$; we denote its covariance matrix by $C(\boldsymbol{\varepsilon})$.

Ideally, \mathbf{k} in equation (1) can represent any model inputs that are incompletely known. Conceptually, there is no
125 limit to the number of elements that comprise the vector \mathbf{k} , and hence to the complexity of model parameterisation. Typically, elements of \mathbf{k} represent spatially distributed hydraulic and transport properties. They may also include historical system stresses, such as pumping and recharge rates that are poorly estimated, as well as some uncertain specifications of other boundary conditions.

130 Suppose the model is run over a period for which predictions are made. Let the vector \mathbf{s} contain simulator predictions of interest. We depict these as being computed from model parameters using the operator \mathbf{Y} . Thus:

$$\mathbf{s} = \mathbf{Y}(\mathbf{k}) \quad (2)$$

Suppose that the model is run N times over its simulation period, and that this simulation period spans both the
135 time over which history-matching is performed (that is, the “calibration period”) and the time over which predictions are required (that is, the “prediction period”); depending on the prediction, these two periods may coincide. Suppose further that on each of the N occasions on which the model is run, the vector \mathbf{k} comprises a different sample of its prior probability distribution of \mathbf{k} . The set of N realisations of \mathbf{o} computed by the model over these N model realisations can be collected into a matrix \mathbf{O} by arranging them in columns. Meanwhile, the
140 set of N realisations of \mathbf{s} in equation (2) can be similarly collected into a matrix \mathbf{S} . From these realisations, vectors depicting the mean of \mathbf{O} and the mean of \mathbf{S} (i.e. $\underline{\mathbf{o}}$ and $\underline{\mathbf{s}}$) are calculated as:

$$\underline{\mathbf{o}} = \frac{\sum_{i=1}^N \mathbf{o}_i}{N} \quad (3a)$$

$$\underline{\mathbf{s}} = \frac{\sum_{i=1}^N \mathbf{s}_i}{N} \quad (3b)$$

145 where \mathbf{o}_i and \mathbf{s}_i in equations (3) depict the i 'th column of \mathbf{O} and \mathbf{S} respectively. Let $\underline{\mathbf{O}}$ and $\underline{\mathbf{S}}$ designate matrices whose columns are comprised of replicates of $\underline{\mathbf{o}}$ and $\underline{\mathbf{s}}$. Consider now the covariance matrix:

$$C\left(\begin{bmatrix} \mathbf{o} \\ \mathbf{s} \end{bmatrix}\right) = \begin{bmatrix} C_{oo} & C_{os} \\ C_{so} & C_{ss} \end{bmatrix} \quad (4)$$

where:

$$C_{oo} = \frac{(\mathbf{o} - \underline{\mathbf{o}})(\mathbf{o} - \underline{\mathbf{o}})^T}{N - 1} \quad (5a)$$

150

$$C_{os} = C_{so}^T = \frac{(\mathbf{o} - \underline{\mathbf{o}})(\mathbf{s} - \underline{\mathbf{s}})^T}{N - 1} \quad (5b)$$

$$C_{ss} = \frac{(\mathbf{s} - \underline{\mathbf{s}})(\mathbf{s} - \underline{\mathbf{s}})^T}{N - 1} \quad (5c)$$

Submatrices appearing on the right side of equation (4) can be calculated from realisations of model outputs using equations (5).

155

Conditioning of predictions by historical observations of system state (see below) often benefits from transforming individual elements o_i and s_i of \mathbf{o} and \mathbf{s} into normally distributed variables o_i^g and s_i^g before calculating the covariance matrices that are depicted in equation (4). Unfortunately, Gaussian transformation of individual elements of \mathbf{o} and \mathbf{s} does not guarantee that the joint probability distribution of $[\mathbf{o}^{gT}, \mathbf{s}^{gT}]$ is multi-
 160 Gaussian. However, this can be at least partially accommodated by undertaking an ensemble-based conditioning process in which \mathbf{o}^g and \mathbf{s}^g are linked by a surrogate model. This is now discussed. Meanwhile, to make the following notations a little less complex, we drop the “g” superscript.

2.2 The DSI Surrogate Model

165

Sun and Durlofsky (2017) and Lima et al. (2020) demonstrate the use of a covariance-matrix-derived surrogate model that can be used to link \mathbf{o} and \mathbf{s} . Conditioning of \mathbf{s} by \mathbf{h} (the measured counterpart of \mathbf{o}) is then achieved by adjusting the parameters of this model using standard parameter conditioning methodologies. The former authors use the randomised maximum likelihood method, while the latter authors use an ensemble smoother.

170

The DSI prediction model is described by the following equation:

$$\begin{bmatrix} \mathbf{o} \\ \mathbf{s} \end{bmatrix} = \begin{bmatrix} \mathbf{o}_p \\ \mathbf{s}_p \end{bmatrix} + C^{1/2} \left(\begin{bmatrix} \mathbf{o} \\ \mathbf{s} \end{bmatrix} \right) \mathbf{x} \quad (6)$$

“Adjustable parameters” of this model comprise the vector \mathbf{x} in equation (6). Meanwhile \mathbf{o}_p and \mathbf{s}_p are prior mean
 175 values of \mathbf{o} and \mathbf{s} . The prior probability distribution of elements x_i of \mathbf{x} is such that they are independently normal with a standard deviation of 1.0. Thus:

$$E(\mathbf{x}) = \mathbf{0} \quad (7a)$$

and

$$C(\mathbf{x}) = \mathbf{I} \quad (7b)$$

180

where $E(\mathbf{x})$ in equation (7a) denotes the expected value of \mathbf{x} and $C(\mathbf{x})$ in equation (7b) denotes the prior covariance matrix of \mathbf{x} . The square root of the covariance matrix that is depicted in equation (6) is obtained using singular value decomposition. First:

$$C \begin{pmatrix} \mathbf{o} \\ \mathbf{s} \end{pmatrix} = \mathbf{U}\mathbf{\Sigma}\mathbf{U}^T \quad (8)$$

185

where \mathbf{U} in equation (8) is an orthonormal matrix and $\mathbf{\Sigma}$ is a diagonal matrix whose elements are positive singular values. The square root of this matrix is then obtained as:

$$C^{1/2} \begin{pmatrix} \mathbf{o} \\ \mathbf{s} \end{pmatrix} = \mathbf{U}\mathbf{\Sigma}^{1/2}\mathbf{U}^T \quad (9)$$

190

Normally $\mathbf{\Sigma}^{1/2}$ in equation (9) is truncated so that unduly low singular values are excluded. The sum of squared singular values (i.e. the diagonal elements of $\mathbf{\Sigma}^{1/2}$) is a measure of the total variability of $\begin{bmatrix} \mathbf{o} \\ \mathbf{s} \end{bmatrix}$. Normally truncation of $\mathbf{\Sigma}^{1/2}$ is such that 99% or more of this variability is retained. Once singular value truncation has been accomplished, a linearised inverse problem can be formulated using the following equation (10). (Without loss of generality, we omit the vector of prior means $\begin{bmatrix} \mathbf{o}_p \\ \mathbf{s}_p \end{bmatrix}$ in this and the following equations to simplify them.)

$$\begin{bmatrix} \mathbf{h} \\ \mathbf{s} \end{bmatrix} = C^{1/2} \begin{pmatrix} \mathbf{o} \\ \mathbf{s} \end{pmatrix} \mathbf{x} + \begin{bmatrix} \boldsymbol{\varepsilon} \\ \mathbf{0} \end{bmatrix} = \mathbf{M}\mathbf{x} + \begin{bmatrix} \boldsymbol{\varepsilon} \\ \mathbf{0} \end{bmatrix} \quad (10)$$

195

The matrix operator \mathbf{M} is defined through the above equation. Let the matrix \mathbf{N} be an appropriate "selection matrix" comprised of 1's and 0's such that:

$$\mathbf{h} = \mathbf{N} \begin{bmatrix} \mathbf{h} \\ \mathbf{s} \end{bmatrix} \quad (11)$$

200 Then:

$$\mathbf{h} = \mathbf{L}\mathbf{x} + \boldsymbol{\varepsilon} \quad (12)$$

where:

$$\mathbf{L} = \mathbf{N}C^{1/2} \begin{pmatrix} \mathbf{o} \\ \mathbf{s} \end{pmatrix} \quad (13)$$

205

In equations (10-12), the vector \mathbf{h} contains measurements of historical system behaviour that correspond to model outputs \mathbf{o} (same as in equation 1). We refer to the model \mathbf{M} herein as the "DSI surrogate model" that links elements of observed system behaviour to elements of its predicted behaviour (normally those that have decision-relevance). As stated above, the former are encapsulated in the vector \mathbf{o} while the latter are encapsulated in the vector \mathbf{s} . This surrogate model can be "calibrated" against field measurements of system state encapsulated in \mathbf{h} to obtain a maximum a posteriori (MAP) estimate $\underline{\mathbf{x}}$ of \mathbf{x} , from which a MAP estimate $\underline{\mathbf{s}}$ of \mathbf{s} can be readily obtained using equation (6). Alternatively, or in addition, samples of the posterior distribution of \mathbf{x} can be obtained using standard Bayesian methods. In the following analysis, we use an ensemble smoother as well as a linearised form of Bayes equation for prediction conditioning. Because the computations embodied in equation (10) are simple, the DSI surrogate model runs extremely fast.

210

215 2.3 Imposition of History-Match Constraints

In the examples that follow, we apply equations (10) and (12) in a number of different ways. These will now be briefly described.

220 The first of these applications is similar to that described by Lima et al. (2020). That is, an ensemble smoother is used to directly sample the posterior probability distribution of \mathbf{x} . The posterior probability distribution of \mathbf{s} is then sampled by running the DSI surrogate model using these samples of \mathbf{x} . We use the PESTPP-IES ensemble smoother described by PEST++ development team (2022) for this purpose.

225 We then use Tikhonov regularised inversion to “calibrate” the surrogate model, thereby obtaining a MAP estimate $\underline{\mathbf{x}}$ of \mathbf{x} from which a MAP estimate $\underline{\mathbf{s}}$ of \mathbf{s} is obtained from a single forward run of the calibrated DSI surrogate model. Calibration is achieved using PEST (Doherty, 2022). Because of equation (6) and the fact that the prior expected value of \mathbf{x} is $\mathbf{0}$, the Tikhonov-regularised solution to the inverse problem described by equation (12) is (Doherty, 2015):

$$230 \quad \underline{\mathbf{x}} = (\mathbf{L}^T \mathbf{Q} \mathbf{L} + \beta^2 \mathbf{I})^{-1} \mathbf{L}^T \mathbf{Q} \mathbf{h} \quad (14)$$

In equation (14), \mathbf{Q} is the observation weight matrix; ideally:

$$\mathbf{Q} = \mathbf{C}^{-1}(\boldsymbol{\epsilon}) \quad (15)$$

235 In practice, equation (14) is solved iteratively as a value for β is sought that guarantees a model-to-measurement least squares objective function that is equal to, or greater than, a user-specified value. This value is calculated from the statistics of measurement noise (de Groot-Hedlin and Constable, 1991; Doherty, 2003).

As explained below, we also use a constrained optimisation process to determine the maximum and minimum values that an individual prediction (i.e. an individual element of \mathbf{s}) can take subject to the constraint that a least squares objective function does not rise above a user-specified value. This objective function is comprised of appropriately-weighted model-to-field-measurement residuals, as well as departures of elements of \mathbf{x} from their prior expected values of $\mathbf{0}$.

240

245 Because the prior expected value of \mathbf{x} is $\mathbf{0}$, we can write:

$$\mathbf{0} = \mathbf{x} + \boldsymbol{\eta} \quad (16)$$

where $\boldsymbol{\eta}$ in equation (16) is a random vector with the same statistical properties as \mathbf{x} . Equation (12) can then be written as:

$$\begin{bmatrix} \mathbf{h} \\ \mathbf{0} \end{bmatrix} = \begin{bmatrix} \mathbf{L} \\ \mathbf{I} \end{bmatrix} \mathbf{x} + \begin{bmatrix} \boldsymbol{\epsilon} \\ \boldsymbol{\eta} \end{bmatrix} \quad (17a)$$

250 With obvious definitions for \mathbf{d} , \mathbf{J} and $\boldsymbol{\tau}$, equation (17a) can be re-written as:

$$\mathbf{d} = \mathbf{J} \mathbf{x} + \boldsymbol{\tau} \quad (17b)$$

From (7b), the covariance matrix of $\boldsymbol{\tau}$ is:

$$255 \quad \mathbf{C}(\boldsymbol{\tau}) = \mathbf{C} \left(\begin{bmatrix} \boldsymbol{\varepsilon} \\ \boldsymbol{\eta} \end{bmatrix} \right) = \begin{bmatrix} \mathbf{C}(\boldsymbol{\varepsilon}) & \mathbf{0} \\ \mathbf{0} & \mathbf{I} \end{bmatrix} \quad (18)$$

Let the vector \mathbf{y} denote the sensitivity of an element s_i of \mathbf{s} to surrogate model parameters \mathbf{x} . For predictive uncertainty analysis, we define a least squares objective function ϕ_u as the sum of squared, weighted model-to-measurement misfit residuals and parameter misfit residuals from their preferred values of $\mathbf{0}$. Thus:

$$260 \quad \Phi_u = (\mathbf{h} - \mathbf{o})^T \mathbf{Q} (\mathbf{h} - \mathbf{o}) + \mathbf{x}^T \mathbf{x} \quad (19)$$

Suppose that values of the objective function ϕ_u in equation (19) that exceed a user-specified value of ϕ_{u0} are deemed to be unlikely (at a certain level of confidence). Vecchia and Cooley (1987) show that solution of the constrained optimisation problem in which s_i is maximized/minimized subject to the constraint that $\phi_u \leq \phi_{u0}$ can
265 be obtained through iterative solution of the following equation (20a):

$$\mathbf{x} = (\mathbf{J}^T \mathbf{Q} \mathbf{J})^{-1} \left\{ \mathbf{J}^T \mathbf{Q} \mathbf{h} - \frac{\mathbf{y}}{2\lambda} \right\} \quad (20a)$$

where:

$$\left(\frac{1}{2\lambda} \right)^2 = \pm \frac{\Phi_{u0} - \mathbf{d}^T \mathbf{R} \mathbf{d} + \mathbf{d}^T \mathbf{R} \mathbf{J} (\mathbf{J}^T \mathbf{R} \mathbf{J})^{-1} \mathbf{J}^T \mathbf{R} \mathbf{d}}{\mathbf{y}^t (\mathbf{J}^T \mathbf{R} \mathbf{J})^{-1} \mathbf{y}} \quad (20b)$$

270 and:

$$\mathbf{R} = \mathbf{C}^{-1}(\boldsymbol{\tau}) \quad (20c)$$

Recall that \mathbf{d} is defined by equation (17b). Maximisation or minimisation of s_i is chosen according to the sign
275 used in equation (20b). In the following example, this process is carried out using the ‘‘predictive analysis’’ functionality of PEST (Doherty, 2022).

Finally, in the examples that we present below, we apply linear uncertainty analysis to evaluate the worth of
280 various subsets of field data (i.e. elements of \mathbf{h}). If we assume a linear relationship between surrogate model outputs (under both history-matching and predictive conditions) and surrogate model parameters, and Gaussian probability distributions for both \mathbf{x} and $\boldsymbol{\varepsilon}$, the posterior uncertainty of a prediction s_i can be calculated from the prior covariance matrix $\mathbf{C}(\mathbf{x})$ of model parameters on the one hand, and the covariance matrix $\mathbf{C}(\boldsymbol{\varepsilon})$ of measurement noise on the other hand using the following Bayes-derived equation (Doherty, 2015; Fienen et al., 2010):

$$285 \quad \sigma_{si}^2 = \mathbf{y}^T \mathbf{C}(\mathbf{x}) \mathbf{y} - \mathbf{y}^T \mathbf{C}(\mathbf{x}) \mathbf{L}^T [\mathbf{L} \mathbf{C}(\mathbf{x}) \mathbf{L}^T + \mathbf{C}(\boldsymbol{\varepsilon})]^{-1} \mathbf{L} \mathbf{C}(\mathbf{x}) \mathbf{y} \quad (21)$$

The first term on the right side of equation (21) is the prior uncertainty of the prediction s_i . The second term represents predictive uncertainty reduction accrued through history-matching. In implementation of equation (21), the sensitivities embodied in the vector \mathbf{L} can be calculated using finite perturbations of the MAP estimate $\underline{\mathbf{x}}$ of \mathbf{x} . Meanwhile $\mathbf{C}(\underline{\mathbf{x}})$ is the identity matrix \mathbf{I} .

It is important to note that equation (21) includes the values of neither parameters nor observations; it features only sensitivities. Hence, as will be discussed below, it can be easily turned to the task of data worth evaluation. In particular, the ability of a new measurement to reduce the uncertainty of a prediction of interest can be evaluated without actually knowing the value of that measurement.

3. Application

The objective of this section is to demonstrate the performance and utility of DSI in quantifying posterior uncertainties of predictions made by a model whose run time is long and whose parameter field is complex. As is common in the literature, where the performance of a new method is tested and documented, we base our analyses on a synthetic model rather than on a real-world model. This allows us to assess, and document the performance of the method. It also dispenses with the need to account for epistemic uncertainties which accompany real-world modelling.

We discuss the application of the DSI methodology in a synthetic alluvial river-aquifer context, a common hydrogeological setting. Alluvial river corridors are used worldwide for drinking water supply. Up to 85% of groundwater withdrawals from these systems come from surface water capture (Scanlon et al., 2023). They provide productive aquifer systems and natural riparian filtration (see, for example, Epting et al. 2022). Alluvial deposits have been formed by millennia of channel meander migration, aggregation and erosional flow processes. These processes result in highly heterogeneous aquifers in which palaeochannels provide preferential flow paths. These preferential flow paths significantly influence the spatial and temporal dynamics of the exchange fluxes between rivers and aquifers. Note that the stochastic characterisation of these subsurface structures is strongly non-Gaussian. This makes it difficult to evaluate the statistical properties of management-pertinent model predictions.

In our synthetic example, the objective of our numerical experiments is to mimic real-world modelling as it is undertaken in many alluvial depositional environments with which we are familiar. The numerical model is therefore constructed to predict surface water infiltration along a river, and surface water travel times to water production wells with particular emphasis on the shortest of these times. Both of these variables are relevant to the management of an alluvial aquifer used for drinking water supply. The provision of these predictions by a numerical model can, for example, assist water managers in operating a well field in a way that minimizes the potential for bacterial contamination of drinking water (Epting et al., 2018). In this example, we investigate the ability of DSI to associate uncertainties with management-pertinent predictions, and to support data acquisition strategies which may further reduce these uncertainties.

3.1 Numerical Model

It is essential to consider interactions and feedback mechanisms between the surface and subsurface when
330 simulating alluvial aquifers that are connected to rivers. Integrated Surface and Subsurface Hydrologic Models
(ISSHMs) provide a consistent framework for simulating flow and transport processes for such systems
(Schilling et al., 2022; Brunner et al., 2017). An important feature of these models is that they can dynamically
simulate feedback between the surface and subsurface water regimes over a wide range of temporal and spatial
scales (Simmons et al., 2020; Paniconi and Putti 2015). The ISSHM modelling platform HydroGeoSphere
335 (HGS) (Aquanty Inc., 2022; Brunner and Simmons 2012; Brunner et al., 2012) is used to perform the numerical
simulations documented herein. HGS simulates surface water (SW) and groundwater (GW) flow processes using
a globally implicit, finite-difference flow formulation. Simulation of water flow within the surface water domain
is based on the 2D diffusion-wave equation, while the three-dimensional, variability-saturated Richards equation
is used to simulate subsurface flow processes.

340

3.2 Model Setup

3.2.1 Geometry

345 The numerical flow model deployed to explore and document the capabilities of DSI has a spatial extent of $300 \times 500 \times 30$ m in the x , y and z directions (Figure 1a). An alluvial plain slopes gently towards the river outlet with
a slope of 0.003 m/m in the y -direction. The river itself flows along the eastern boundary of the model domain in
a 3 m deep and 15 m wide channel. The numerical grid is discretised using a 2D unstructured triangular mesh
with lateral internodal spacing that ranges between 4 m along the river and 7 m under the proximal alluvial plain.
350 The 2D mesh was generated using AlgoMesh (HydroAlgorithmics Pty Ltd, 2022). The model has 14 layers.
Layer boundaries are at depths of 0.5, 1.0, 1.5, 2.0, 3.0, 4.0, 5.0, 8.0, 11.0, 14.0, 17.0, 20.0, 23.0 and 26.0 metres.
The bottom of the model is at a depth of 30 metres. The resulting 3D mesh consists of 112,240 nodes and
204,000 elements (or cells).

3.2.2 Boundary conditions

The surface water inflow on the upstream side of the river is conceptualised through a second type (specified
flux) boundary corresponding to a constant flow (Q) of $7200 \text{ m}^3 \cdot \text{h}^{-1}$. The surface water outflow is implemented
as a so-called “critical depth boundary”, which allows surface water to leave the overland flow area downstream
360 (Figure 1a). Meanwhile, an areal infiltration rate of $300 \text{ mm} \cdot \text{y}^{-1}$ is imposed over all nodes of the alluvial plain
that borders the river. This top boundary condition represents effective rainfall, as evapotranspiration processes
are not explicitly simulated by the model. At the northern and southern ends of the groundwater system, a head-
dependent (Cauchy-type) boundary condition is deployed to ensure regional groundwater in- and outflow at
these upstream and downstream model boundaries respectively. Lateral model boundaries, as well as the basal
365 model boundary, are impermeable.

Two production wells are represented by nodal flux boundary conditions; each well extracts $400 \text{ m}^3 \cdot \text{h}^{-1}$ from the
groundwater system. In each well the pump is placed at an elevation of 85 m (i.e. at a depth of approximately 14
m). As in all ISSHMs, streamflow simulation is explicit. The exchange between the surface and the subsurface is
370 based on the heads calculated for the two flow domains and a coupling length between them (the so-called dual-
node approach). For this example, we use a coupling length of 0.1 m.

The simulation covers a period of 460 days. Over this period, the model runs for 365 days for the initialisation of hydraulic conditions. Then, over the next 95 days, extraction rates from the two water production wells are varied to mimic a controlled pumping experiment (Figure 1b). During this experiment, well field extraction is shut down for 50 days. The pumping rate is then restored to its initial value of $400 \text{ m}^3 \cdot \text{h}^{-1}$ per well, and the simulation continues for another 30 days. This pumping rate reduction experiment introduces significant transience to the groundwater system. The induced transience has the potential to provide a significant amount of information on the hydraulic properties of the system. This setup is loosely based on a real-world experiment that was conducted in the Aeschau plain, Switzerland (Schilling et al., 2017).

The average computational time required for the model to simulate the transient simulation is 10 minutes; the simulation is not parallelized. HGS employs adaptive time-stepping; however the maximum time step is limited to a single day in order to ensure numerical stability.

385

3.2.3 Parameterisation

The generation of realistic distributions of subsurface hydraulic properties in depositional environments that are characterised by distinct, continuous features of complex geometry such as alluvial channels, is often implemented using rule-based feature-generation codes. Alternatively, packages which implement multiple-point geostatistics (Remy et al., 2009; Linde et al., 2015) can be employed. Algorithms that underpin the former codes generate structures that can have similar geometric properties to alluvial channels, whereas the latter packages employ stochastic image analysis techniques to reproduce these structures while maintaining hydraulic property connectedness.

395

In the present case, we employed the ALLUVSIM alluvial channel simulator (Pyrce et al., 2009) to generate distributions of the alluvial subsurface. (Note that the distribution of the alluvial channels does not affect the present location of the river; conceptually they are remnants of historical river channels). The numerical generation of superimposed and intersecting alluvial channels is controlled by geometric (and stochastic) input parameters such as channel depth, width, porosity, starting location and sinuosity (Pyrce et al., 2009); see Table 1. ALLUVSIM simulations were used to assign sets of alluvial channels to the HGS groundwater flow domain.

For the generation of ALLUVSIM channel sets we adopted a width-to-depth ratio of 1. Furthermore, the depth of channel deposits averages 20m, this being a considerable portion of the modelled subsurface. Recall that the depth of the base of the model is 30m. We do not stack channels at different depths. Therefore, each distribution of the subsurface contains a small number (up to 10) of alluvial channels, each of which is continuous from the north to the south of the model domain, while extending from the surface to a depth that approaches the bottom of the alluvium. As is apparent in Table 1, the mean channel x coordinate (about 370 m from the western edge of the ALLUVSIM model boundary along its northern boundary) is such that channels tend to occupy parts of the subsurface that are not too far from the course of the present river. Groundwater flow within the near-river part of the model domain is therefore dominated by the presence of these continuous, conductive channels. One of the ALLUVSIM-generated channel distributions (out of a total of 101) was adopted as the “reality” channel distribution. This is displayed in Figure 1c. The other 100 channel distributions were used to generate

410

realisations of prior hydraulic properties in the HGS groundwater flow domain. These prior realisations are
415 required by the DSI process described above.

Prior realisations of hydraulic properties contain three facies; these facies are channel, non-channel and riverbed
deposits. This last facies is present below the current river location and develops in the upper layer of the HGS
model to a depth of 50 centimetres. For each HGS model realisation, each of these facies was provided with a
420 spatially uniform set of hydraulic properties (i.e. hydraulic conductivity and porosity). The value of each of these
properties was randomly selected from probability distributions that are presented in Table 1. (Intra-facies
heterogeneity was purposefully neglected to examine DSI's performance in geological settings where hydraulic
properties are categorical, with one category exerting a dominant influence on groundwater flow.) Appendix A
depicts a number of HGS model parameter realisations, coloured according to horizontal hydraulic conductivity.

425

A vertical anisotropy of 4 was assigned to all hydraulic conductivities in all realisations. This is consistent with
alluvial depositional systems similar to those that our study attempts to represent. (Gianni et al., 2018; Chen
2000; Ghysels et al., 2018).

430 Parameters that govern unsaturated flow are homogeneous, and invariant between realisations. The van
Genuchten-Mualem parameters a [m^{-1}] and β [-] were set to 3.48 and 1.75, respectively, these being typical of
alluvial gravel (Dann et al., 2009). The residual soil water content was set to 0.095. The Manning's roughness
coefficient was set to $1.7 \times 10^{-6} \text{ d.m}^{-1/3}$.

435 3.3 History-matching dataset and model predictions

The dataset used for history matching consists of 95 observations of hydraulic heads in each of the eight
observation wells, providing a total of 760 individual observations. These heads were calculated using the HGS
"reality parameter field". A random realisation of measurement noise was added to each head measurement. The
440 probability density distribution of synthetic head measurement noise has a mean of 0.0m and a standard
deviation of 0.05m. Figure 2 shows "reality heads" together with heads calculated at the same locations using the
remaining 100 hydraulic property realisations. There is considerable scatter in these plots. This suggests that the
information content of these heads concerning subsurface hydraulic properties is high. Their information content
with respect to predictions of interest is pursued using the methodologies discussed above.

445

The predictions of interest are as follows:

- fast travel times (days) at the first well (well #1);
- fast travel times (days) at the second well (well #2);
- rate of surface water infiltration into the groundwater system (l.s^{-1}) along the entire length of the river.

450

Travel times are calculated using particles; see Anderson et al. (2015) for details. For each realisation of the
alluvial architecture and accompanying hydraulic properties, particles are placed along the riverbed at the top of
the subsurface flow domain; see Figure 1c. Most particles leave the model domain through one of the two
extraction wells. The travel time that corresponds to the 5th percentile of the particle breakthrough curve at a

455 particular well under normal operating conditions is deemed to be the “fast travel time” pertaining to that well. Our focus on fast-moving water acknowledges the likelihood of rapid flow processes being driven by preferential flow paths. These same rapid flow processes can threaten water extraction in the event of surface water contamination.

460 Fast times and surface water infiltration are calculated at $t = 365$ days. Thus they pertain to maximum well abstraction rates.

For the synthetic reality, the 5th percentile of travel times is 9.57 and 7.90 days for water production wells #1 and #2, respectively. Meanwhile, surface water infiltration along the entire river is 130.67 l.s^{-1} .

465

4. Uncertainty Quantification

In this section, we document how the posterior (i.e. post-history-matching) uncertainties of the three predictions of interest can be evaluated using four different approaches. One of these requires adjustment of the parameters of the HGS model. The other three approaches require adjustment of parameters of a surrogate model that is built to implement DSI-based predictive uncertainty evaluation in ways that are discussed in Section 2. In all cases parameter adjustment minimizes a least squares objective function that serves as a measure of model-to-measurement misfit. This objective function is calculated as the sum of weighted squared differences between observed and modelled heads in the eight observation wells discussed above. Weights are uniform to reflect the temporal uniformity of measurement noise; each has a value that is equal to the square of the standard deviation of this noise. The expected value of the history-matched objective function is therefore expected to be somewhat greater than 760, this being the number of observations which comprise the calibration dataset. The “somewhat greater” is an outcome of the fact that number of “effective parameters” is unknown prior to solving an ill-posed inverse problem; see Doherty (2015) for details.

480

4.1 Bayesian history-matching

4.1.1 History matching with the HGS model

485 Prior to using DSI for the exploration of predictive uncertainty, we adjust HGS model parameters using the PESTPP-IES ensemble smoother. History-match-constrained parameter fields were then used to make the predictions of interest. The variability of these predictions between these posterior parameter fields is a measure of their posterior uncertainties.

490 The ensemble smoothing process begins with samples of the prior parameter probability distribution. In the present case, we used the 100 parameter fields that were obtained in the manner discussed above. These parameter fields are iteratively adjusted until model outputs fit field measurements. The HGS model has 204,000 adjustable elements, these being hydraulic conductivities and porosities ascribed to individual model cells. As is common practice when using parameter ensembles for history-matching, each of these is considered a separate parameter when undertaking PESTPP-IES-based parameter adjustment.

495

Piecewise spatial uniformity of the initial parameter fields is lost during the ensemble parameter adjustment process as each parameter is subject to individual adjustment while maintaining a high level of spatial correlation with neighbouring parameters that is inherited from the initial realisations. See Chen and Oliver
500 (2013) for mathematical details of the parameter adjustment process.

The objective function associated with all ensemble realisations was significantly reduced after 3 iterations of the IES parameter adjustment process. Objective function values ranged between 1075 and 16098, except for 30 realisations which suffered excessively slow HGS model solution convergence and were therefore abandoned.
505 Note that each iteration of the IES parameter adjustment process requires as many model runs – in this case HGS model runs - as there are realisations that comprise the ensemble. Figure 2 shows that model-calculated heads at the observation wells are indeed close to “measured” heads. The 70 realisations which remained after 3 IES iterations were used to make the predictions that are described above. The results are plotted in Figure 3a.

510 It can be seen from Figure 3a that the uncertainty of predicted surface water infiltration is significantly reduced by PESTPP-IES based history matching of the HGS model. It can therefore be concluded that the information content of hydraulic heads with respect to this specific prediction is high. In contrast, the uncertainties of first arrival travel time predictions are not significantly reduced; see Figure 3a. The information content of head responses to altered pumping rates with respect to these predictions is therefore lower than it is for surface water
515 infiltration.

An interesting feature of Figure 3a is that some posterior parameter fields have fast travel times that exceed those calculated using prior parameter fields. This can be explained by the fact that some posterior parameter fields have lost some of the connectivity exhibited by the prior parameter fields. (see Appendix B). This is an outcome
520 of the PESTPP-IES parameter adjustment process which is only truly Bayesian where prior parameter distributions are Gaussian on a cell-by cell basis (if cell-by-cell parameterisation is employed). However, the prior realisations that compose the initial ensemble from which the IES inversion process has started is not multiGaussian (see Appendix A). Neither the theory on which IES is based, nor numerical implementation of that theory in its history-matching algorithm, can guarantee the maintenance of long-distance hydraulic property
525 connectedness which cannot be characterised by a multiGaussian distribution. Indeed, history-match-constrained adjustment of connected and categorical parameter fields is still an area of active research (Khambhammettu et al., 2020). Note that while uncertainty analysis methods such as rejection sampling or Markov Chain Monte Carlo approaches do not require a Gaussian prior nor a Gaussian likelihood function, these methods are impractical in contexts where the number of parameters is high and model run times are long, which is the case
530 for the many hydrogeological applications and for the example used in this paper.

4.1.2 History matching with the DSI surrogate model

The same 100 samples of the prior parameter probability distribution that were used to start the PESTPP-IES
535 data assimilation process were then used to construct a DSI surrogate model using the methodology described in Section 2. Recall that this surrogate model is based on an empirical covariance matrix that relates history-matched model outputs to predictive model outputs. A singular value energy level of 0.999 was used in the

construction of this surrogate model. This results in the use of 87 singular values (and corresponding eigencomponents) of this matrix, and hence an 87-dimensional \mathbf{x} vector; see equation (6). Note that the only
540 HGS model runs that were required to construct and history-match the DSI surrogate model were those that were based on the 100 prior hydraulic property field realisations discussed above. No further runs of the HGS model were required to carry out any of the procedures described below.

Sampling of the posterior distribution of surrogate model parameters (i.e. elements of the \mathbf{x} vector) was
545 implemented using the PESTPP-IES ensemble smoother. However, in contrast to the previous use of PESTPP-IES, its use with the DSI surrogate model incurs a trivial numerical burden because of the extremely fast execution speed of this model. An ensemble comprising 100 realisations of the prior probability distribution of surrogate model parameters was adjusted. After 6 iterations of this process, all realisations yielded good model-to-measurement fits, with objective function values ranging between 814 and 830. Prior and posterior prediction
550 histograms are shown in Figure 3b.

The posterior prediction probability distributions for surface water infiltration calculated by HGS parameter adjustment on the one hand, and by DSI surrogate model parameter adjustment on the other hand are very similar. The same cannot be said for fast travel times. The posterior uncertainty of this prediction is lower after
555 DSI surrogate model parameter adjustment than after HGS model parameter adjustment. This suggests that estimation of DSI surrogate model parameters does not suffer the same degradation in uncertainty evaluation performance as that which is incurred by PESTPP-IES-based adjustment of HGS parameters which tend to lose their continuity as the history-matching process progresses. In contrast, parameters of the DSI surrogate model are not required to maintain any spatial patterns or relationships; they must simply represent observation-to-
560 prediction relationships that are embodied in 100 HGS model outputs that were all calculated using continuous hydraulic property parameter fields.

4.2 Tikhonov-regularised inversion and constrained predictive maximization/minimization

565 The DSI surrogate model was calibrated using Tikhonov regularisation; see equation (14). The MAP estimates of \mathbf{x} obtained in this way were used to calculate MAP values of predictions. These are listed in Appendix C.

Following calibration of the DSI surrogate model, equation (21) was used to calculate the prior and posterior standard deviations of the uncertainties of the three predictions of interest based on an assumption of surrogate
570 model linearity. Sensitivities of model outputs that correspond to members of the calibration dataset, and that correspond to model predictions, were calculated using finite difference perturbations from calibrated surrogate model parameter values. Linear-calculated standard deviations were then used to plot the probability density distributions for the three predictions so that they can be compared with ensemble-calculated standard deviations (Figure 3c).

575 Next, posterior uncertainties of the three predictions of interest were calculated using the constrained maximisation/minimisation procedure that is described by equation (20). The objective function constraint provided to this equation was that which enables the calculation of Scheffe 95% confidence intervals (see

580 Vecchia and Cooley, 1987). The values obtained through this process agree reasonably well with maximum and minimum predictions obtained through Bayesian history matching of the DSI surrogate model (Figure 3c).

585 Differences between evaluated predictive uncertainties that appear in Figure 3 (statistics are available in Appendix C) are generally small; however some are large enough to warrant discussion. Differences between linear and nonlinear uncertainty estimates can be at least partly attributed to approximations that calculation of these estimates require. Linear estimation of posterior predictive uncertainty requires not only an assumption of linearity of the DSI model; it also assumes Gaussianity of the prior probability distributions of DSI model parameters (i.e. elements of the \mathbf{x} vector of equation 6). Meanwhile, nonlinear analysis, involving adjustment of HGS model parameters by PESTPP-IES is prone to sampling errors incurred through the use of only 100 realisations; it is also affected by problems that beset PESTPP-IES in maintaining continuity of hydraulic properties (see above). Another factor that may degrade the accuracy of posterior uncertainties calculated using the HSG model is failure of model outputs based on some parameter realisations to fit measured heads to within limits that are set by the statistical properties of measurement noise. Nevertheless, in spite of these approximations, it is pleasing to note that the ratio of prior to posterior uncertainty is reasonably consistent between all linear and nonlinear estimates of posterior predictive uncertainty. This increases confidence in the data worth analysis which is the subject of the next section.

595

5. Data worth

600 Quantifying the effectiveness and efficiency of existing and planned data acquisition and monitoring strategies can (and often should) be an important outcome of decision-support groundwater modelling. This is because quantification of uncertainty brings with it an ancillary benefit, this being quantification of the extent to which existing or anticipated data acquisition can reduce the uncertainties of one or more decision-critical model predictions. The worth of data increase in proportion to their ability to achieve this outcome.

605 5.1 Worth of existing data

The worth of data, and subsets thereof, that already comprise the calibration dataset can be evaluated according to two different metrics. The worth of subsets of existing data can be assessed by evaluating the extent to which the posterior standard deviations of decision-critical model predictions are increased by their omission from this dataset. The worth of these subsets can also be assessed by evaluating the extent to which the prior standard deviation of these predictions is reduced by including a particular subset as the only member of the history-matching dataset. In the present section, we evaluate the worth of existing data according to the first of these metrics only. This is implemented using linear analysis based on equation (21). It is worth noting that, because the surrogate model runs so fast, the ensemble smoother could also have been used to sample the posterior distribution of our predictions with the omission of certain subsets of the history-matching dataset.

615

Using equation (21), data is notionally omitted in a calibration dataset simply by setting their associated weights to values of zero. This was done for each of the observation wells that are featured in Figure 1a. The outcomes of this analysis are presented in Figure 4.

620

Inspection of Figure 4 reveals that members of the existing observation network are more informative of predictive flux than they are of fast travel times. Furthermore, the cost of omitting OBS110 from the existing observation network appears to be greater than that of omitting any other observation well from the network. This implies a certain degree of uniqueness of information that is forthcoming from this well. This is not surprising as OBS110 is located upstream and closer to sources of surface water infiltration than most of the other observation wells. It is therefore close to the path of much of the water that flows from the river to production wells.

625

Of particular interest is the high information content of OBS17 data with respect to the prediction of induced infiltration. This is attributable to the fact that prior realisations of hydraulic properties display spatial uniformity within each stratigraphic unit (that is channels, riverbed and other alluvium). Therefore, while pumping-induced surface water infiltration is sensitive to the structure and disposition of paleochannels which convey water from the river to production wells, it is also sensitive to aquifer properties that can control inflow/outflow of water to/from the northern and southern boundaries of the model domain. The difference in head between OBS17 and the southern head-dependent boundary is informative of these properties. The importance of these head measurements would be reduced if stratigraphic unit properties were internally heterogeneous.

630

635

5.2 Worth of a new observation point

Equation (21) can be readily turned to evaluation of the issue of whether it is worth supplementing the existing observation network of eight observation wells with a new observation well. In our study, contenders for the new observation point are each of the 146 sites that are represented by black crosses in Figure 1a. We establish the worth of including a new point in the monitoring network by including heads at that point in an expanded history-matching dataset, thereby assuming that observations from this well were available during the calibration period that has formed the basis for all investigations that have been discussed so far. The reduction in the uncertainty standard deviation of management-pertinent predictions that is accrued through expansion of the history-matching dataset in this way is a measure of the worth of the hypothesized new data. Recall from the discussion in Section 2 of this paper, that equation (21) does not require the values of observation to assess their worth. It requires only the sensitivities of corresponding model outputs to model parameters.

645

650

We base our exploration of data worth on a DSI surrogate model. However, HGS model outputs on which this model is based must be extended to include those at the candidate observation wells. This enables the construction of an expanded covariance matrix that links model outputs at these sites to predictions of interest. In our case, these were available from archived output files of the 100 HGS model runs which form the basis for results that are reported in previous sections of this paper. In other cases, another suite of large model runs may be required for the construction of a new surrogate model. Note, however, that once these model runs have been completed, all further analyses can be conducted using the DSI surrogate model.

655

To verify this linear approach to data worth assessment, reductions in predictive uncertainty that would result from updating the calibration dataset to include heads from each of the 146 potential observation wells that are shown in Figure 1a were calculated using an alternative (and much more laborious) nonlinear approach.

For each of the 100 prior realisations of HGS parameter fields, heads were calculated at each of the 146 trial observation points. For each of these observation points, for each of these parameter realisations, a new DSI model was constructed using the methodology discussed above. The history-matching dataset for each of these models included the existing dataset (comprised of eight observation wells), as well as the expanded dataset that is pertinent to that well and that particular realisation of the prior HGS parameter field. Predictions were the same for each DSI surrogate model (i.e. fast travel times to the production wells and surface water infiltration). Each of these 14,600 DSI surrogate models was then history-matched against its respective history-matching dataset to obtain the posterior uncertainties of our predictions of interest. This was done using the PESTPP-IES ensemble smoother. For each trial observation well, the “total” posterior uncertainty of a prediction of interest was calculated by accumulating prediction realisations over all 100 DSI surrogate models that pertained to each expanded observation well. These were compared with the posterior uncertainties calculated using the original DSI surrogate model that was based on a history-matching dataset that did not include the new well.

For both approaches, the percent reduction in the standard deviations of the uncertainties of our predictions were calculated for each of the 154 observation wells. These were then interpolated over the model grid for presentation purposes; see Figure 5.

Areas of high and low worth of installation of a new observation well are broadly similar between the upper and lower sets of maps that comprise Figure 5, especially for the surface water infiltration prediction.

It is clear from Figure 5 that the collection of new hydraulic head data in the northern part of the model has the potential to reduce the uncertainty associated with predictions of surface water infiltration. This also applies to fast travel times to the northern extraction well, and to a lesser extent for fast travel times to southern extraction well. The nonlinear analysis also suggests that acquisition of head data in the river corridor between the existing OBS110 and OBS83 observation wells may yield reductions in uncertainties of fast travel time predictions for both water production wells. To a lesser extent (especially for the southern production well), this is also established through linear analysis. This makes sense, as this zone is crossed by most of the particles that arrive at the production wells.

Both methods for data worth analysis that are described above are based on approximations. Nonlinear analysis suffers from the limited number of realisations on which it is based. Obviously, linear analysis suffers from an assumption of DSI surrogate model linearity. Nevertheless, despite these approximations, the two approaches yield results that are in broad agreement with each other. Furthermore, they are both readily deployable in real-world contexts where hydraulic property distributions and processes are complex; this applies especially to DSI-based linear analysis.

6. Discussion and Conclusions

700

The purpose of this paper is to document and demonstrate the use of data space inversion (DSI) as a means of quantifying and reducing the posterior uncertainties of predictions made by complex models with complex parameter fields. Both model attributes make application of traditional uncertainty analysis difficult. Model complexity increases model run time; it can also increase the propensity of a model to exhibit unstable numerical

705 behaviour when endowed with a stochastic parameter field. The complexity of parameterisation, especially when it involves the use of continuous, connected hydraulic properties (as illustrated in our example), can violate the assumptions upon which these properties are adjusted in order for model outputs to respect measurements of system behaviour.

710

Data space inversion addresses the first of these challenges by replacing a numerical model with a fast-running DSI surrogate model. This surrogate model is tuned to the decision-support role for which the original, complex model was built. This is because the DSI surrogate model is designed to replicate the ability of a numerical model to simulate past measurements of system behaviour and to make predictions of future system behaviour that are of interest to management. Both of these complex model outputs can be calculated using parameter

715 fields of arbitrary complexity that represent aspects of the subsurface that are critical to past and future groundwater behaviour. In many cases, these will include structural or alluvial features that can rapidly transport water and dissolved contaminants to points of environmental impact.

720

Realisations that compose the initial ensemble from which model outputs are calculated do not have to be multiGaussian. The multiGaussian assumption used to link measurements of past system behaviour to predictions of future system behaviour is independent of any assumptions about the prior realisations. Because a direct link is made between measurements and predictions (thereby bypassing parameters), an assumption of multiGaussianity is likely to have a weaker effect on the results of the predictive uncertainty analysis process than highly parameterised methods that rely implicitly or explicitly on parameter adjustment (such as linear

725 Bayesian methods, randomised maximum likelihood methods and iterative ensemble smoother methods). Thus, prior realisations used to start the DSI process can accommodate both aleatory and epistemic uncertainties. Uncertainties in prior parameter distributions can also be readily accommodated.

730

A strength of the DSI methodology is that it does not require adjustment of hydraulic property fields for model outputs to replicate the past so that they can be used as a basis for posterior sampling of future groundwater behaviour. Instead, the parameters and predictions of a DSI surrogate model (rather than the original model) are subjected to adjustment and posterior sampling. The nature of these surrogate model parameters is such that they embody the parameterisation complexity of the original model without replicating it. Instead, they are formulated to reproduce the effects of that complexity on the model outputs used for both history matching and

735 system management. Thus, the complex nuances of system hydraulic properties are implicitly taken into account as predictions of future system behaviour are conditioned by measurements of past system behaviour.

This paper demonstrates that the use of a DSI surrogate model can extend beyond that of sampling the posterior probability distribution of one or several predictions of interest. Like a conventional numerical model, it can be

740 used for rapid assessment of the worth of existing or new data. The simplest (and most rapid) form of data worth
analysis relies on an assumed linear relationship between surrogate model parameters and surrogate model
outputs. There may be many circumstances where this linearity assumption is more applicable than that of a
linear relationship between conventional model parameters and conventional model outputs, as the latter
relationships are bypassed in definition and construction of the DSI surrogate model and its parameters. DSI-
745 based evaluation of data worth may therefore be more reliable than evaluation of data worth using a complex
model. In fact, if a complex model has many parameters (as it should), and its run times are high (as they often
are), calculation of sensitivities that are required for linear analysis may not be possible. Meanwhile, by
construction, the parameters of a DSI surrogate model can take the complex dispositions and connectivity
relationships of real-world hydraulic properties into account.

750

This paper also demonstrates more complex uses to which a DSI surrogate model can be put. Tikhonov-
regularised inversion and constrained, nonlinear prediction optimisation are demonstrated in Section 4. Section 5
demonstrates how more complex assessments of data worth can be made than that which relies on an assumption
of surrogate model linearity. While the numerical costs associated with these assessments are high, they are far
755 from prohibitive.

However, together with strength comes weakness. It is acknowledged that while the DSI methodology enables
rapid and effective posterior uncertainty analysis in contexts that may otherwise render such analyses
approximate at best and impossible at worst, a modeller is entitled to feel a sense of frustration at not being able
760 to “see for him/herself” the parameter fields that give rise to predictive extremes. Not only may an understanding
of these fields add to a modeller’s understanding of a system; they may accomplish the same thing for decision-
makers and stakeholders as well.

Code availability

765 The DSI source code that was used to implement analyses that are described herein can be downloaded from a public data repository (<https://doi.org/10.5281/zenodo.7913402>). Data used for this study are available in a public data repository (<https://doi.org/10.5281/zenodo.7707975>).

Author contribution

770 HD and PB designed the synthetic numerical experiment. JD implemented the DSI method in PEST. JD performed the linear analysis using the DSI-based model. HD performed the non-linear analysis using the DSI-based model. HD wrote the first draft. JD and PB collaborated with HD on this first draft. PB secured the funding for HD. HD ensured quality of the final paper.

Competing interests

775

The authors declare that they have no conflict of interest

Acknowledgements

780 The authors acknowledge the funding provided by the Swiss National Science Foundation (SNF, grant number 200021_179017) and the GMDSI project (see <https://www.gmsi.org>). The authors would like to thank Jeremy T. White for his helpful feedback on early versions of our paper. The authors would like to thank an anonymous reviewer and Jasper A. Vrugt for their comments on the preprint.

References

785

Anderson MP, Woessner WW and Hunt RJ.: Applied groundwater modeling: simulation of flow and advective transport. Academic, Cambridge, MA, 2015.

Aquanty Inc. HydroGeoSphere Theory Manual. Waterloo, ON. p. 101, 2022.

790 Brunner, P., Doherty, J., and Simmons, C. T.: Uncertainty assessment and implications for data acquisition in support of integrated hydrologic models. *Water Resources Research*, 48, W07513, doi:10.1029/2011WR011342, 2012.

Brunner, P., and Simmons, C. T.: HydroGeoSphere: a fully integrated, physically based hydrological model. *Groundwater* 50, 170–176, doi:10.1111/j.1745-6584.2011.00882.x, 2012.

795 Brunner, P., Therrien, R., Renard, P., Simmons, C. T., and Hendricks Franssen, H. J. : Advances in understanding river-groundwater interactions. *Reviews of Geophysics*, 55, 818–854, doi:10.1002/2017RG000556, 2017.

Chen, X. : Measurement of streambed hydraulic conductivity and its anisotropy. *Environmental Geology*, 39,12, doi:10.1007/s002540000172, 2000.

800 Chen, Y. and Oliver, D. S.: Levenberg–marquardt forms of the iterative ensemble smoother for efficient history matching and uncertainty quantification. *Computational Geosciences*, 17(4):689–703, doi : 10.1007/s10596-013-9351-5, 2013.

Dann, R., Close, M., Flintoft, M., Hector, R., Barlow, H., Thomas, S and Francis, G.: Characterization and estimation of hydraulic properties in an alluvial gravel vadose zone. *Vadose Zone Journal*, 8(3):651—663, 2009.

805 Dausman, A.M., J. Doherty, C.D. Langevin, and M.C. Sukop.: Quantifying data worth toward reducing predictive uncertainty. *Groundwater* 48, no. 5: 729–740, doi: 10.1111/j.1745-6584.2010.00679.x, 2010.

de Groot-Hedlin, C and Constable, S.: Occam’s inversion to generate smooth, two-dimensional models from magnetotelluric data. *Geophysics* (12):1613-1624, doi : 10.1190/1.1442813, 1991.

810 Delottier, H., Therrien, R., Young, N. L., and Paradis, D.: A hybrid approach for integrated surface and subsurface hydrologic simulation of baseflow with Iterative Ensemble Smoother. *Journal of Hydrology*, 606. doi:10.1016/j.jhydrol.2021.12740, 2022.

Doherty, J.: Ground water model calibration using pilot points and regularisation. *Groundwater*, doi : 10.1111/j.1745-6584.2003.tb02580.x, 2003.

815 Doherty, J.: Calibration and uncertainty analysis for complex environmental models. Published by Watermark Numerical Computing, Brisbane, Australia. 227pp. ISBN: 978-0-9943786-0-6. Downloadable from www.pesthomepage.org, 2015.

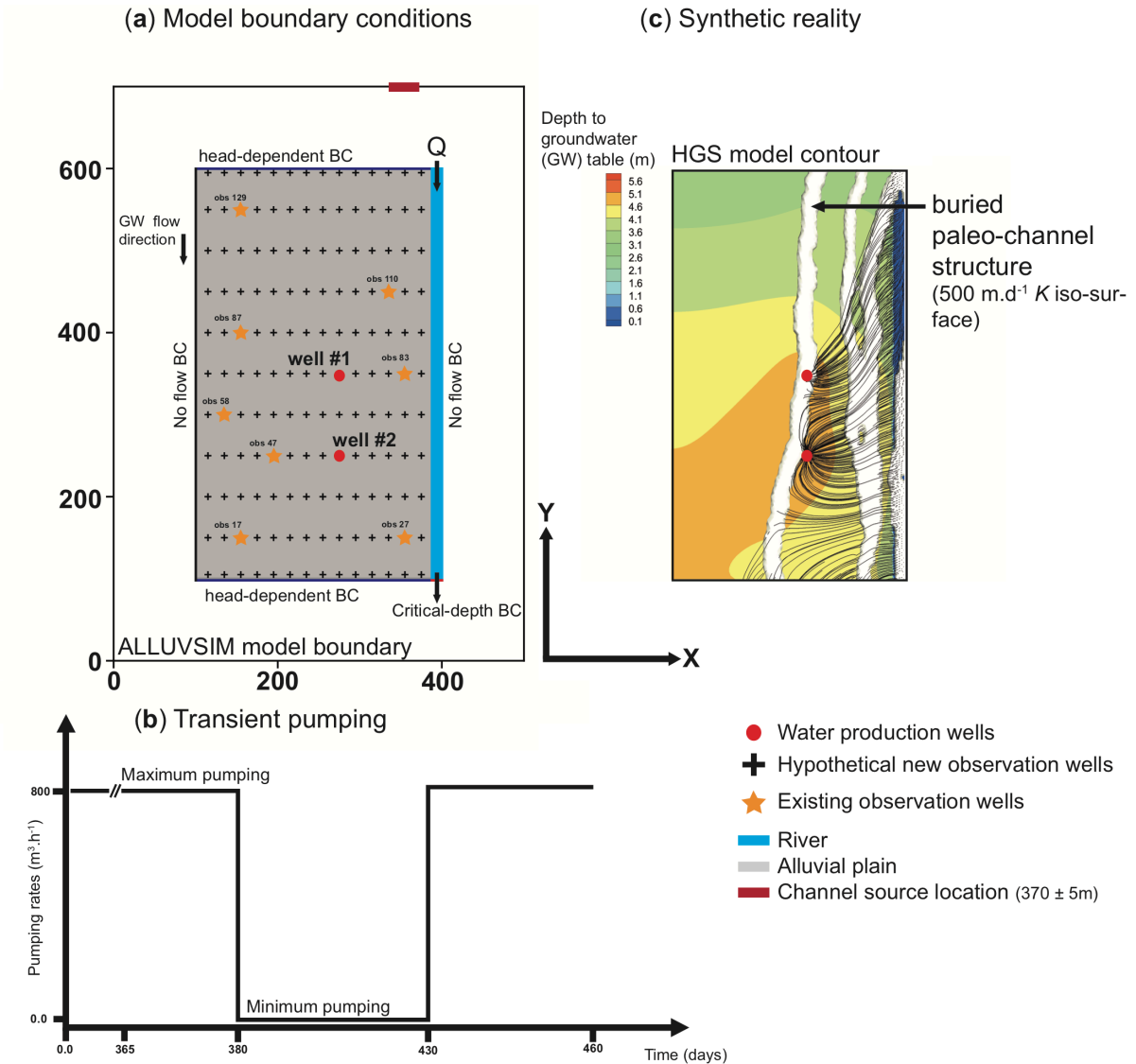
Doherty, J. and Moore, C.: Decision support modeling: data assimilation, uncertainty quantification, and strategic abstraction. *Groundwater* 58, 327–337. doi. org/10.1111/gwat.12969, 2020.

820 Doherty, J.: Manual for PEST. Watermark Numerical Computing. Downloadable from <http://www.pesthomepage.org>, 2022.

Epting, J., Huggenberger, P., Radny, D., Hammes, F., Hollender, J., Page, R.M., Weber, S., Bänninger, D., and Auckenthaler, A.: Spatiotemporal scales of river-groundwater interaction – The role of local interaction

- processes and regional groundwater regimes. *Sci. Total Environ.* 618, 1224–1243. <https://doi.org/10.1016/j.scitotenv.2017.09.219>, 2018.
- 825 Epting, J., Vinnaa, L.R., Piccolroaz, S., Affolter, A. and Scheidler, S.: Impacts of climate change on Swiss alluvial aquifers--A quantitative forecast focused on natural and artificial groundwater recharge by surface water infiltration. *Journal of Hydrology X*. 17(100140), doi:10.1016/j.hydroa.2022.100140, 2022.
- Fienen, M. N., Doherty, J., Hunt, R. J., and Reeves, J.: Using prediction uncertainty analysis to design hydrologic monitoring networks: Example applications from the Great Lakes water availability pilot project (Vol. 2010–5159. Reston, Virginia, USA: USGS, 2010.
- 830 Ghysels, G., Benoit, S., Awol, H., Jensen, E. P., Debele Tolche, A., Anibas, C., and Huysmans, M.: Characterization of meter-scale spatial variability of riverbed hydraulic conductivity in a lowland river (Aa River, Belgium). *Journal of Hydrology*, 559, 1013–1027, doi:10.1016/j.jhydrol.2018.03.002, 2018.
- Gianni, G., Doherty, J., and Brunner, P.: Conceptualization and calibration of anisotropic alluvial systems: Pitfalls and biases. *Groundwater*, doi:10.1111/gwat.12802, 2018.
- 835 He, J., Sarma, P., Bhark, E., Tanaka, S., Chen, B., Wen, X-H., Kamath, J.: Quantifying expected uncertainty reduction and value of information using ensemble-variance analysis. *SPE J.* 23, 428–448, doi:10.2118/182609-PA, 2018.
- Hermans T.: Prediction-focused approaches: an opportunity for hydrology. *Groundwater* 55:683–687, doi: 10.1111/gwat.12548, 2017.
- 840 HydroAlgorithmics Pty Ltd. AlgoMesh User Guide. Melbourne, VIC. 2022.
- James, S.C., J. Doherty, and A.-A. Eddebarh.: Practical Postcalibration uncertainty analysis: Yucca Mountain, Nevada, USA. *Groundwater* 47, no. 6: 851–869., doi:10.1111/j.1745-6584.2009.00626.x, 2009.
- Juda, P., Straubhaar, J., and Renard, P.: Comparison of three recent discrete stochastic inversion methods and influence of the prior choice. *Compt. Rendus. Géosci.* 355, doi: 10.5802/crgeos.160, 2022.
- 845 Khambhammettu, P., Renard, P., and Doherty, J.: The Traveling Pilot Point method. A novel approach to parameterize the inverse problem for categorical fields. *Advances in Water Resources*, 138, 103556. doi:10.1016/j.advwatres.2020.103556, 2020.
- Kikuchi, C.: Toward increased use of data worth analyses in groundwater studies. *Groundwater* 55 (5), 670–673., doi: 10.1111/gwat.12562, 2017.
- 850 Lam, D.-T., Kerrou, J., Renard, P., Benabderrahmane, H., and Perrochet, P.: Conditioning multi-gaussian groundwater flow parameters to transient hydraulic head and flowrate data with iterative ensemble smoothers: a synthetic case study. *Front. Earth Sci.* 8:202, doi: 10.3389/feart.2020.00202, 2020.
- Lima, M.M., Emerick, A.A. and Ortiz, C.E.P.: Data-space inversion with ensemble smoother. *Comput. Geosci.* 24, 1179-1200, doi:10.1007/s10596-020-09933-w, 2020.
- 855 Linde, N., P. Renard, T. Mukerji, and J. Caers, Geological realism in hydrogeological and geophysical inverse modeling: A review, *Adv. Water Resour.*, 86, 86–101, doi:10.1016/j.advwatres.2015.09.019, 2015.
- Paniconi, C., and Putti, M.: Physically based modeling in catchment hydrology at 50: survey and outlook. *Water Resour. Res.* 51, 7090–7129, doi: 10.1002/2015WR017780, 2015.
- 860 PEST++ Development Team. Manual for PEST++. Downloadable from <https://github.com/usgs/pestpp>, 2022.
- Pyrcz, M.J., Boisvert, J.B. and Deutsch C V. ALLUVSIM: A program for event-based stochastic modeling of fluvial depositional systems. *Comput Geosci* ;35:1671–85, doi :10.1016/j.cageo.2008.09.012, 2009.

- Remy, N., Boucher, A. and Wu, J.: Applied Geostatistics with SGeMS: A User's Guide. Cambridge University Press, 2009.
- 865 Satija, A. and Caers, J.: Direct forecasting of subsurface flow response from non-linear dynamic data by linear least-squares in canonical functional principal component space. *Adv. Water Resour.* 77, 69–81, doi:10.1016/j.advwatres.2015.01.002, 2015.
- Scanlon, B.R, Fakhreddine, S., Rateb, A., de Graaf, I., Famiglietti, J., Gleeson, T., Grafton, R.Q.; Jobbagy, E., Kebede, S., Kolusu, S.R. and others: Global water resources and the role of groundwater in a resilient water future. *Nature Reviews Earth & Environment*. 1—15, doi :10.1038/s43017-022-00378-6, 2023.
- 870 Scheidt C, Jeong C, Mukerji T and Caers J.: Probabilistic falsification of prior geologic uncertainty with seismic amplitude data: application to a turbidite reservoir case. *Geophysics*; 80M89–M12, doi:10.1190/geo2015-0084.1., 2015.
- Schilling, O. S., Gerber, C., Purtschert, R., Kipfer, R., Hunkeler, D., and Brunner, P.: Advancing physically-based flow simulations of alluvial systems through atmospheric noble gases and the novel ³⁷Ar tracer method. *Water Resour. Res.* 53, 10465–10490. doi: 10.1002/2017WR020754, 2017.
- 875 Schilling, O. S., Partington, D. J., Doherty, J., Kipfer, R., Hunkeler, D. and Brunner, P: Buried paleo-channel detection with a groundwater model, tracer-based observations and spatially varying, preferred anisotropy pilot point calibration. *Geophys. Res. Lett.* doi: 10.1029/2022GL098944, 2022.
- 880 Simmons, C. T., Brunner, P., Therrien, R., Sudicky, E. A: Commemorating the 50th anniversary of the Freeze and Harlan (1969) *Blueprint for a physically-based, digitally-simulated hydrologic response model*. *Journal of Hydrology*. 584, 2020.
- Sun, W. and Durlofsky, L. J.: A new data-space inversion procedure for efficient uncertainty quantification in subsurface flow problems. *Math. Geosci.* 49(6), 679–715, doi:10.1007/s11004-016-9672-8, 2017.
- 885 Tonkin, M.J., and J. Doherty.: Calibration-constrained Monte Carlo analysis of highly parameterized models using subspace techniques. *Water Resources Research* 45:W00B10, doi :10.1029/2007WR006678, 2009.
- Vecchia, A.V. and Cooley, R.L.: Simultaneous confidence and prediction intervals for nonlinear regression models with application to a groundwater flow model. *Water Resour Res*, 23 (7), 1237-1250, doi:10.1029/WR023i007p01237, 1987.
- 890 Vrugt, J.A. : Markov chain Monte Carlo simulation using the DREAM software package: Theory, concepts, and MATLAB Implementation. *Environ. Model. Software* 75, 273–316. doi: 10.1016/j.envsoft.2015.08.013, 2016.
- White, J.T.: A model-independent iterative ensemble smoother for efficient history-matching and uncertainty quantification in very high dimensions. *Environmental Modelling and Software* 109, 191-201, doi:10.1016/j.envsoft.2018.06.009, 2018.
- 895

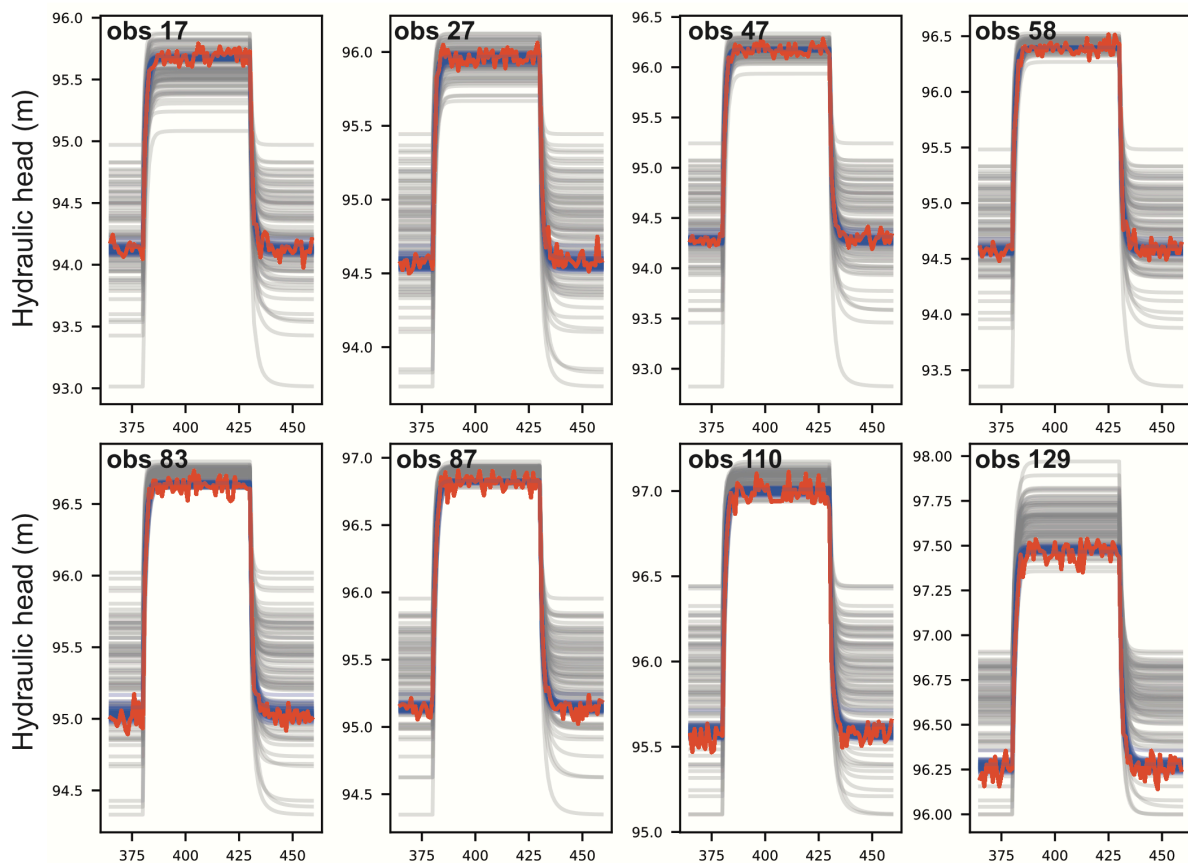


900

Figure 1: (a) Model boundary conditions and observation points that are discussed herein. (b) Transient pumping rates for the two production wells over a period of 95 days; note that the pumping rate is reduced to zero for a period of 50 days. (c) “Synthetic reality” showing “true” alluvial channels that govern hydraulic properties such as hydraulic conductivity and porosity. Depth to groundwater table under the maximum pumping regime is also shown. So too are the paths of particles (black lines converging towards water production wells) that are used to calculate travel times to water production wells.

Table 1: Model parameters used for the synthetic reality, and prior parameter means and uncertainties used for prior ensemble generation.

Parameter type	Unit	Synthetic reality	Priors mean	Prior standard deviation
HydroGeoSphere				
Riverbed Porosity	(-)	0.4	0.20	0.05 (log)
Riverbed Hydraulic conductivity	(m.d ⁻¹)	2.5	5.0	0.20 (log)
Aquifer Porosity	(-)	0.09	0.10	0.05 (log)
Aquifer Hydraulic conductivity	(m.d ⁻¹)	176	150.0	0.10 (log)
Paleo-Channel Porosity	(-)	0.3	0.3	0.05 (log)
Paleo-Channel Hydraulic conductivity	(m.d ⁻¹)	866	1000.0	0.10 (log)
ALLUVSIM				
Channel level elevation	(m)	90	-	
Channel depth	(m)	20	20	3
Channel source location	(m)	370	370	5
Width-to-depth ratio	(-)	1	-	
Channel sinuosity	(-)	0.1	0.1	0.015
Net-to-gross ratio	(-)	0.05	-	
Maximum number of streamlines	(-)	10	-	



910 Figure 2: Observations of hydraulic heads (red); these are calculated by the “Synthetic reality” of the HGS parameter field. Heads calculated by the remaining realisations are shown in grey. Heads calculated using posterior hydraulic property realisations are shown in blue; there are 70 of these.

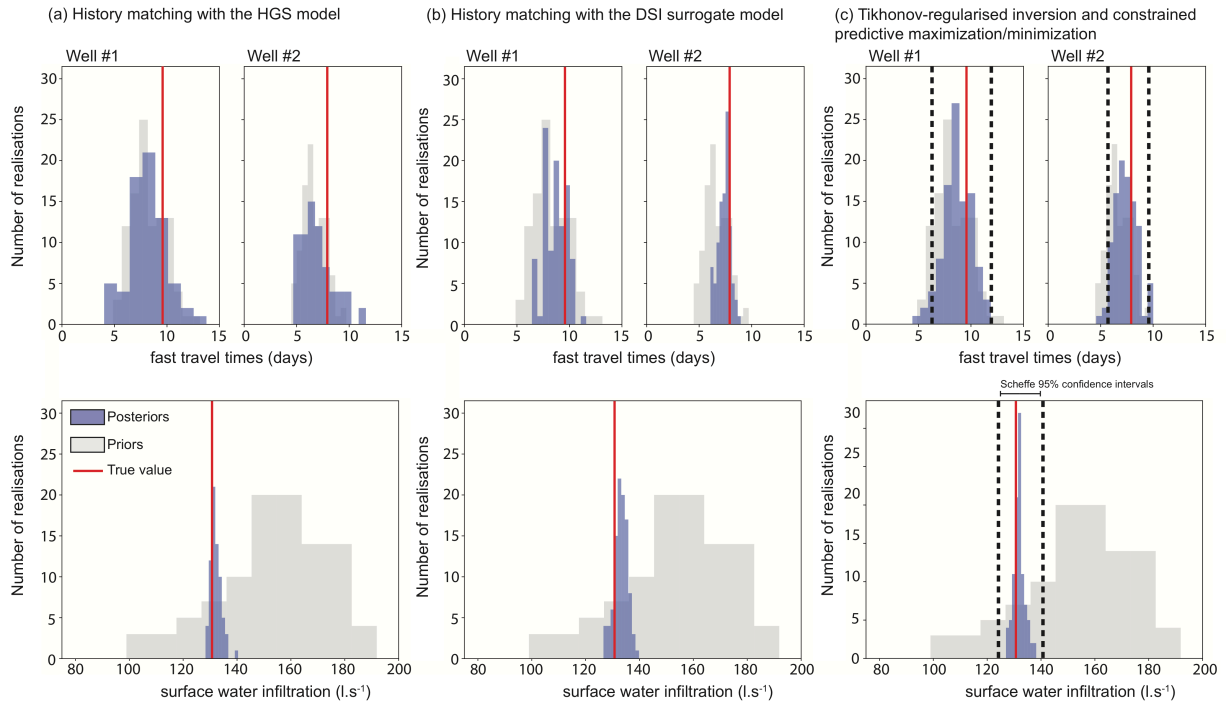
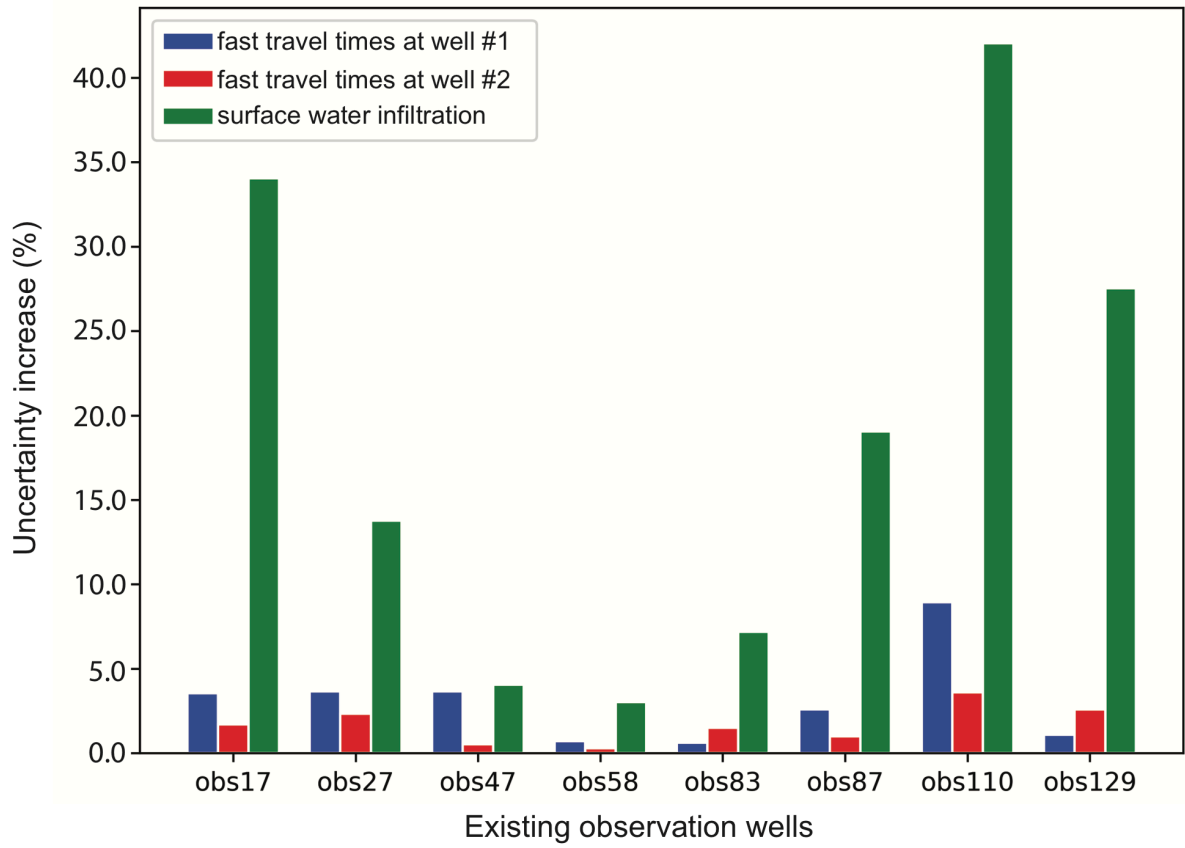
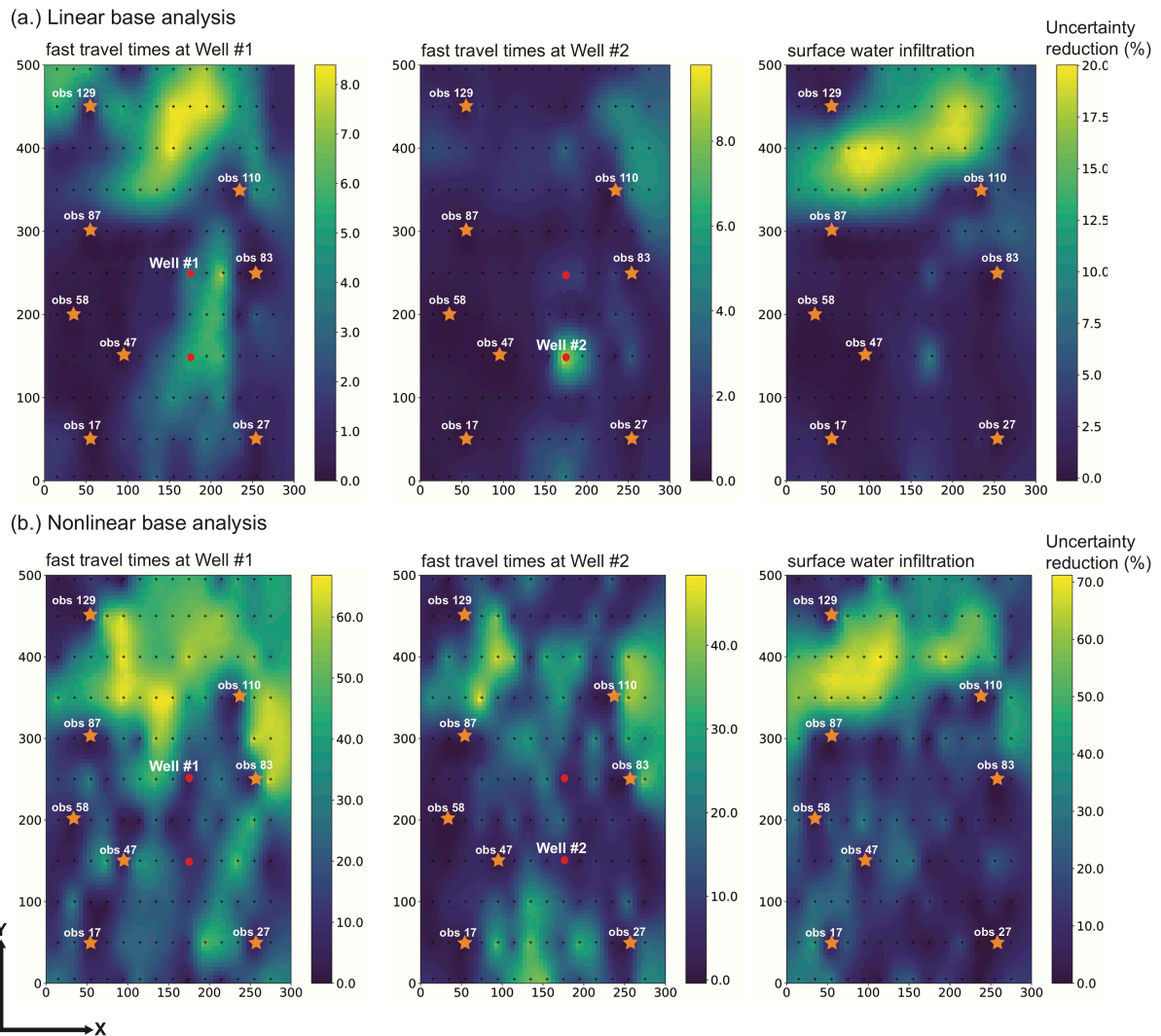


Figure 3: Posterior distributions of model predictions of fast travel times (days) and surface water infiltration (l.s⁻¹) with (a) application of IES (after 3 iterations) to the HydroGeoSphere (HGS) model ensemble (b) application of IES (after 6 iterations) to the surrogate model ensemble and (c) application of equation (21) (linear analysis) and equation (20) (nonlinear analysis) with the MAP estimate of the DSI surrogate model. The dashed lines in (c) represent values for the Scheffe 95% confidence intervals.

920



925 **Figure 4: Percent increase in the standard deviation of posterior uncertainty of each of the three predictions discussed herein when one existing observation well is removed from the current observation dataset.**



930 **Figure 5: Percent decrease in posterior uncertainty of each of the three predictions accrued through supplementing the existing calibration dataset with head measurements gathered in an extra well following (a) linear analysis and (b) nonlinear analysis.**

935 **Appendix A: Prior realisations of alluvial structural features**

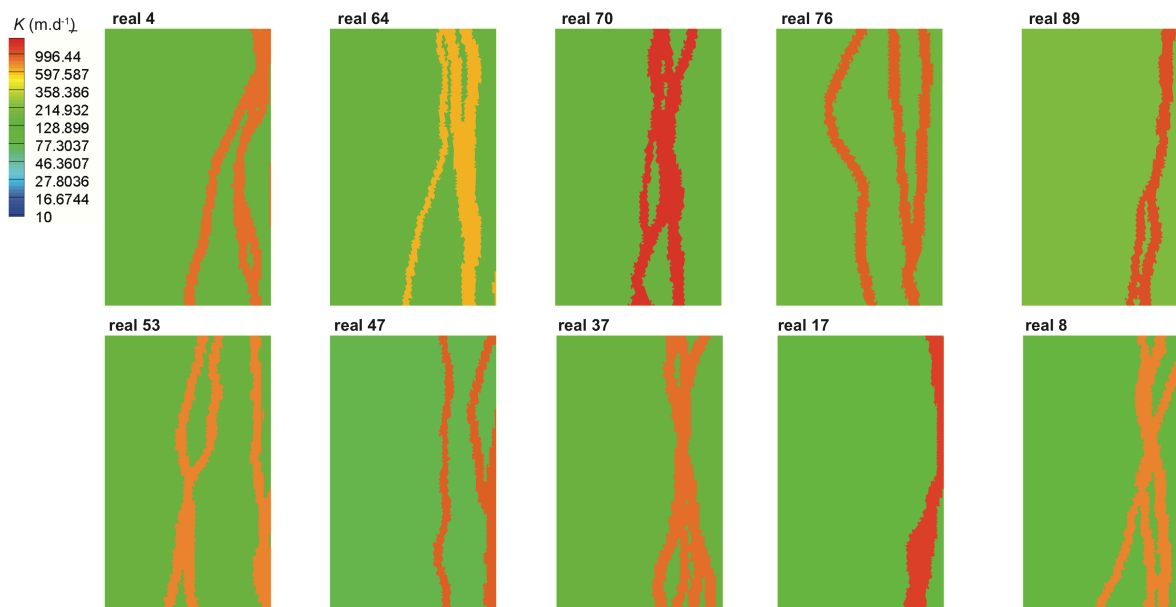


Figure A1. Prior realisations of alluvial structural features generated from ALLUVSIM and mapped into the HGS model for hydraulic conductivity (K) parameterisation.

940 **Appendix B: Posterior estimates of hydraulic conductivity fields**

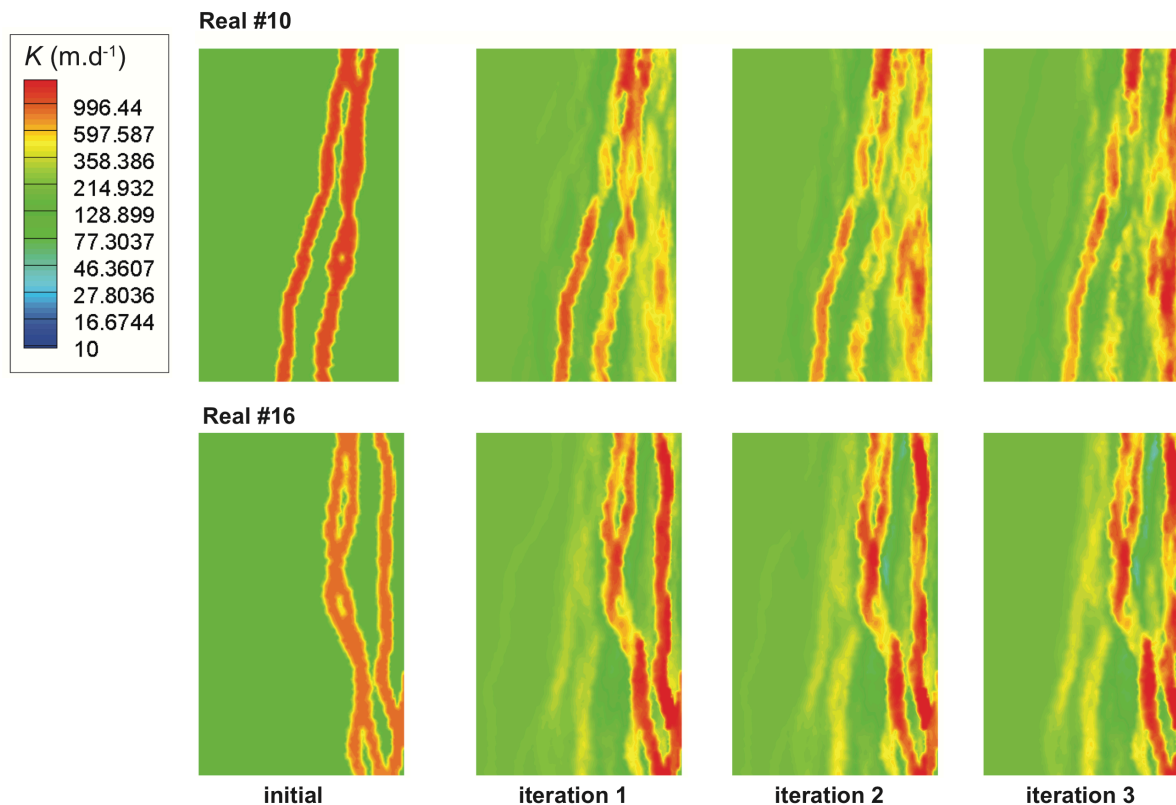


Figure B1. Posterior estimates (for realisations number 10 and 16) of hydraulic conductivity (K) after applying the Iterative Ensemble Smoother over three iterations by adjusting the HGS model parameters with the existing dataset.

Appendix C: Posterior uncertainty statistics

Table C1. Posterior uncertainty statistics of distributions shown in Figure 3.

		Bayesian history- matching on HGS model	Bayesian history- matching on DSI model	MAP estimates on DSI model	Nonlinear analysis on DSI model	Linear analysis on DSI model
HGS model calls		1000	100	100	100	100
fast travel times for well #1 ("reality" = 9.57 days)	Min	4.82	6.59		6.24	
	Max	11.86	10.50		11.89	
	Mean	8.13	8.65	8.63		
	Std	1.63	1.00			1.44
fast travel times for well #2 ("reality" = 7.90 days)	Min	4.67	6.23		5.65	
	Max	9.95	8.52		9.54	
	Mean	6.82	7.36	7.42		
	Std	1.37	0.52			0.94
surface water infiltration ("reality" = 130.67 l.s ⁻¹)	Min	128.30	128.33		124.06	
	Max	135.89	137.98		140.58	
	Mean	131.94	133.27	131.90		
	Std	1.67	2.21			2.15